





Local chirality at exceptional points in optical whispering-gallery microcavitiesJunda Zhu ^{1,2}, Changqing Wang,³ Can Tao ⁴, Zhoutian Fu,³ Haitao Liu ^{4,*}, Fang Bo,^{1,†} Lan Yang,^{3,‡}
Guoquan Zhang,^{1,§} and Jingjun Xu ^{1,¶}¹The MOE Key Laboratory of Weak Light Nonlinear Photonics, TEDA Institute of Applied Physics and School of Physics, Nankai University, Tianjin 300457, China²College of Physics and Materials Science, Tianjin Normal University, Tianjin 300387, China³Department of Electrical and Systems Engineering, Washington University, St. Louis, Missouri, USA⁴Tianjin Key Laboratory of Micro-scale Optical Information Science and Technology, Institute of Modern Optics, College of Electronic Information and Optical Engineering, Nankai University, Tianjin 300350, China

(Received 21 June 2022; revised 12 March 2023; accepted 20 September 2023; published 12 October 2023)

We study the field chirality at the exceptional points (EPs) in an optical whispering gallery mode (WGM) microcavity, which is commonly believed to be globally perfect. We have discovered a locally imperfect or locally perfect chirality of eigenmodes at the EPs in a WGM microcavity perturbed by two strong nanoscatterers. We find that the generally local and imperfect chirality at the EPs tends to be globally perfect with the decrease of the scattering effect induced by the nanoscatterers, and the chirality also becomes locally perfect with the decrease of the relative azimuthal angle between the two strong nanoscatterers. With a first-principles-based model considering a dynamic multiple-scattering process of the azimuthally propagating modes (APMs), all the above counterintuitive phenomena of imperfect or perfect chirality can be respectively explained by a strong or weak frequency dependence of the APM scattering coefficients at an effective scatterer composed of the two nanoscatterers. In this paper, we provide increased understanding of the general properties of chirality at EPs which will benefit potential applications enabled by the chirality features of non-Hermitian systems at EPs.

DOI: [10.1103/PhysRevA.108.L041501](https://doi.org/10.1103/PhysRevA.108.L041501)

Introduction. Exceptional points (EPs) [1,2] are spectral degeneracies in the parameter space of a non-Hermitian system, at which the eigenstates and their associated eigenvalues coalesce. EPs have been studied in various physical platforms ranging from atom systems [3], atom-cavity systems [4], acoustic systems [5], and optical systems [6] to optomechanical systems [7]. In optical systems, unique features at EPs have been utilized for enhanced sensing [8–10], laser linewidth broadening [11], asymmetric mode switching [12–14], etc.

Chirality is one of the unique features at an EP and in general means a specific phase relation between two dominant states in a non-Hermitian system [15,16]. For an optical whispering-gallery-mode (WGM) microcavity system, chirality means a resonant/eigenmode with a dominant clockwise (CW) or counterclockwise (CCW) rotation [17]. By introducing parity-time symmetric refractive index modulation [18], judiciously deforming the shape of the microcavity [17], or tuning light scattering within the mode volume of the microcavity [19,20], one can steer the system to an EP and achieve degenerate eigenmodes with strong spatial chirality. Owing to the chirality at the EP, numerous interesting

phenomena and applications have been demonstrated, such as orbital angular momentum lasing [18], chiral lasing [20], chiral absorbing [21,22], and electromagnetically induced transparency [23,24].

Authors of previous works have predicted that the chirality is globally perfect at the EP in an optical WGM microcavity perturbed by two weak nanoscatterers with an effective non-Hermitian Hamiltonian approach [19]. A globally perfect chirality implies that there only exists a pure CW or CCW WGM component in the resonant modes over the whole azimuthal range of $[0, 2\pi]$ and is regarded as a criterion of the EP in the experiment [8,20,25]. In this letter, we will demonstrate that the chirality of the resonant modes at the EP is generally local and imperfect and could become globally or locally perfect conditionally.

Here, we consider a two-dimensional cylindrical microcavity [26] (with radius R_0) perturbed by two nanoholes [27] inside the microcavity to induce a strong scattering effect (see Supplemental Material (SM) Sec. 1 [28]). As illustrated in Fig. 1(a), two sectorial-shaped [26] nanoholes with different radial lengths r_j ($j = 1, 2$), azimuthal ranges θ_j , and distances d_j away from the cavity boundary are considered.

Definition of the local chirality. To define the local chirality of the electromagnetic field in different azimuthal regions divided by the two nanoholes, we introduce azimuthally propagating modes (APMs) [26,29] and the effective scatterer [26].

(i) APM is a waveguide mode with an electromagnetic field defined on the cross-section of $\phi = \text{const}$. Therefore,

*liuht@nankai.edu.cn

†bofang@nankai.edu.cn

‡yang@seas.wustl.edu

§zhanggq@nankai.edu.cn

¶jjxu@nankai.edu.cn

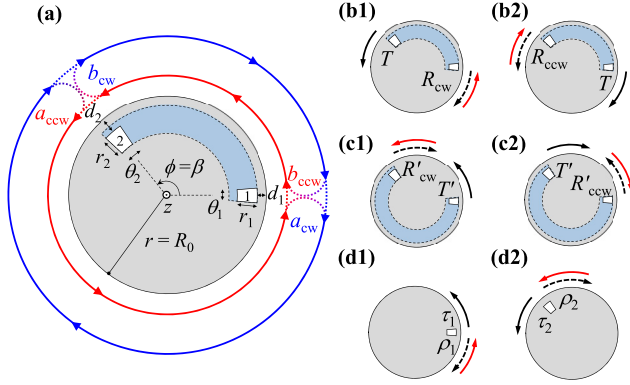


FIG. 1. (a) Schematic of a z -invariant cylindrical microcavity with two nanoholes. r and ϕ denote the radial and azimuthal coordinates, respectively. The blue region represents the effective scatterer. $a_{\text{ccw(cw)}}$ and $b_{\text{ccw(cw)}}$ denote the complex-amplitude coefficients of the azimuthally propagating modes (APMs) outside and inside the effective scatterer, respectively. (b1) and (b2) Definition of the effective reflection (R_{cw} or R_{ccw}) and transmission (T) coefficients of the APM at the effective scatterer with an incident normalized counter-clockwise (CCW) or clockwise (CW) APM, respectively. (c1) and (c2) Like (b1) and (b2) but for a complementary effective scatterer. (d1) and (d2) Fundamental reflection (ρ_j) and transmission (τ_j) coefficients of the APM at the nanohole $j = 1$ and 2 , respectively. The incident APM is denoted by a solid red arrow, while the solid and dashed black arrows in (b1) to (d2) indicate the transmitted and reflected APMs, respectively.

the APM can have different coefficients in different azimuthal regions divided by the two nanoholes and thus can be used as a local basis to describe the local chirality. Differently, WGM, the basis adopted in previous works [19–21,23], is a resonant mode (i.e., the quasinormal mode [30,31] with discrete complex eigen/resonance frequencies) in an unperturbed microcavity and thus is defined over the whole azimuthal range of $\phi \in [0, 2\pi]$. Therefore, the WGM has a unique coefficient over $\phi \in [0, 2\pi]$ and thus acts as a global basis and cannot describe the local chirality. Here, we consider the two counterpropagating APMs [26,29] that form the pair of degenerate WGMs under the resonance condition [32].

(ii) A single effective scatterer is defined as the two nanoholes along with the azimuthal region between them, as illustrated by the blue region in Fig. 1(a) [26]. Then the electromagnetic field of the resonant mode can be expressed as a superposition of the CCW and CW APMs:

$$\Psi_{\text{out}}(r, \phi) = \left(\frac{a_{\text{ccw}}}{v}\right) \Psi_{\text{ccw}}(r, \phi) + a_{\text{cw}} \Psi_{\text{cw}}(r, \phi) \quad (1)$$

outside the effective scatterer, and

$$\Psi_{\text{in}}(r, \phi) = b_{\text{ccw}} \Psi_{\text{ccw}}(r, \phi) + \left(\frac{b_{\text{cw}}}{w}\right) \Psi_{\text{cw}}(r, \phi) \quad (2)$$

inside the effective scatterer, where $\Psi_{\text{ccw}}(r, \phi) = \Psi_{\text{ccw}}(r) \exp(ik_0 n_{\text{eff}} R_0 \phi)$ and $\Psi_{\text{cw}}(r, \phi) = \Psi_{\text{cw}}(r) \exp[ik_0 n_{\text{eff}} R_0 (2\pi - \phi)]$, with $\Psi = [\mathbf{E}, \mathbf{H}]$ denoting both the electric (\mathbf{E}) and the magnetic (\mathbf{H}) vectors of the CCW and CW traveling APMs, respectively, $k_0 = \omega/c$ (with ω and c being the complex resonance angular frequency and the speed of light in the vacuum, respectively), and n_{eff} is the

complex effective index of the APM. Here, a_{ccw}/v , a_{cw} , b_{ccw} , and b_{cw}/w are the complex-amplitude coefficients of APMs normalized at $\phi = 0$. Also, $v = \exp(ik_0 n_{\text{eff}} R_0 \beta)$ and $w = \exp[ik_0 n_{\text{eff}} R_0 (2\pi - \beta)]$ are the propagation factors of the APM traveling azimuthally over the range inside (from 0 to β) and outside (from β to 2π) the effective scatterer, respectively.

Then the local chirality outside and inside the effective scatterer can be defined as

$$\alpha_{\text{out}} = \frac{|a_{\text{ccw}}/v|^2 - |a_{\text{cw}}|^2}{|a_{\text{ccw}}/v|^2 + |a_{\text{cw}}|^2}, \quad \alpha_{\text{in}} = \frac{|b_{\text{ccw}}|^2 - |b_{\text{cw}}/w|^2}{|b_{\text{ccw}}|^2 + |b_{\text{cw}}/w|^2}, \quad (3)$$

respectively. The values of $\alpha_{\text{out(in)}}$ are within $[-1, 1]$, and $\alpha_{\text{out(in)}} = \pm 1$ implies a perfect chirality with a pure CCW (for $+$) or CW (for $-$) APM, respectively [20].

Local and imperfect chirality at EPs. First, we study the impact of the nanohole size on the chirality $\alpha_{\text{out(in)}}$ at an EP. In the following calculation, the refractive indices of the microcavity, the nanoholes and the surrounding medium are set to be 2, 1 and 1 (air), respectively. Other parameters are $R_0 = 1.6 \mu\text{m}$, $d_1 = 0.04 \mu\text{m}$, and $d_2 = 0.0480 \mu\text{m}$, with r_2 gradually increasing from $r_{2,0} = 0.108816 \mu\text{m}$ to $3r_{2,0}$, and $\theta_j = 2\arcsin(r_j/4R_0)$ ($j = 1, 2$). Note that $r_2 = r_{2,0}$ corresponds to the case of weak scattering, and the scattering effects of the nanohole become stronger with the increase of r_2 (see SM Sec. 1.3 [28]). Here, we consider the resonant modes corresponding to the unperturbed WGMs with electric vector along the z direction, an azimuthal number $m = 16$, a resonance wavelength $\sim 1 \mu\text{m}$, and a quality factor (Q) $\sim 10^5$.

By simultaneously scanning r_1 (around r_2) and β ($\sim 130^\circ$; see SM Sec. 2.3 [28]) with the other parameters fixed, an EP is found when the eigenfrequencies of a pair of resonant modes become degenerate and their corresponding waveform patterns become identical. The rigorous numerical results of $\alpha_{\text{out(in)}}$ can be obtained by extracting the APM coefficients with the mode-orthogonality theorem [33] from the electromagnetic field of resonant modes, which are solved with the full-wave finite-element method (FEM) performed by COMSOL Multiphysics software [26,29].

Figure 2(a) shows that, for the EP achieved with relatively weak scatterers, the local chiralities outside (circles) and inside (squares) the effective scatterer are both almost perfect (at $r_2 = r_{2,0}$, for instance, $\alpha_{\text{out}} = -0.9987$ and $\alpha_{\text{in}} = -0.9949$). Consequently, the electric-field intensities outside and inside the effective scatterer both exhibit a traveling wave pattern, as shown in the first column in Fig. 2(b). This is consistent with the globally perfect chirality ($\alpha_{\text{out}} = \alpha_{\text{in}} = \pm 1$) reported in previous literature [19–21,23] for weak scatterers.

However, for the EPs achieved with strong scatterers (at $r_2 = 3r_{2,0}$, for instance), the chiralities outside and inside the effective scatterer both become imperfect. Particularly, the local chirality within the larger azimuthal range divided by the two scatterers is stronger, i.e., $|\alpha_{\text{in}}| < |\alpha_{\text{out}}| < 1$. Accordingly, the electric-field intensities exhibit a quasistanding wave pattern formed by two counterpropagating APMs, and this is less remarkable within the larger azimuthal range divided by the two scatterers. This local and imperfect chirality at EPs for strong scatterers is quite different from the globally perfect chirality for weak scatterers.

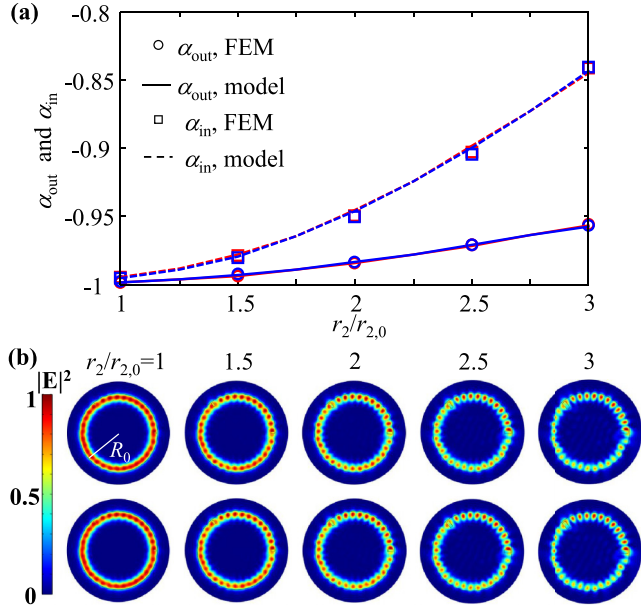


FIG. 2. (a) Local chiralities $\alpha_{\text{out(in)}}$ at the exceptional points (EPs) plotted as functions of size r_2 of nanohole 2. The circles and squares show the finite-element method (FEM) results of α_{out} and α_{in} , respectively. The solid and dashed curves show the model prediction of α_{out} and α_{in} , respectively. The blue and red curves show the results of the pair of nearly degenerate resonant modes. (b) Electric-field intensity distribution at the EPs obtained with the FEM shown in (a). The five columns are for different r_2 , and the two rows are for the pairs of nearly degenerate resonant modes.

Locally perfect chirality at EPs. Second, we study the impact of the relative azimuthal angle β between two strong scatterers on the chirality $\alpha_{\text{out(in)}}$ at EPs. The parameters (see SM Sec. 2.3 [28]) in the following calculation are the same as those in Fig. 2, except that r_2 is fixed at a relatively large value of $2.5r_{2,0}$ to form a strong scattering.

Figure 3(a) shows that, for the EPs achieved at large β , the local chiralities outside (circles) and inside (squares) the effective scatterer are both imperfect, and there is $|\alpha_{\text{in}}| < |\alpha_{\text{out}}| < 1$, like the case in Fig. 2(a). For instance, $\alpha_{\text{out}} = -0.9514$ and $\alpha_{\text{in}} = -0.9286$ for $\beta \sim 174^\circ$. Consequently, the electric-field intensities outside and inside the effective scatterer at EPs do not possess an ideal traveling wave pattern, as shown in the last column in Fig. 3(b) (more results for different β can be found in SM Sec. 5 [28]).

However, for the EPs achieved at small β , Fig. 3(a) shows that α_{out} tends to be perfect ($|\alpha_{\text{out}}| \approx 1$), while α_{in} is weaker ($|\alpha_{\text{in}}| < 1$), which implies a tendency of locally perfect chirality. For instance, for the EP with $\beta = 29.43^\circ$, Fig. 3(a) shows that $\alpha_{\text{out}} = -0.9978$ and $\alpha_{\text{in}} = -0.8087$. Accordingly, the electric-field intensity outside the effective scatterer exhibits a distinct traveling wave pattern. In contrast, the field intensity inside the effective scatterer does not, as shown in the first column in Fig. 3(b). This locally perfect chirality is entirely different from the globally perfect chirality ($\alpha_{\text{out}} = \alpha_{\text{in}} = \pm 1$) for weak scatterers, as shown in Fig. 2 and from the commonly reported results in previous literature [19–21,23].

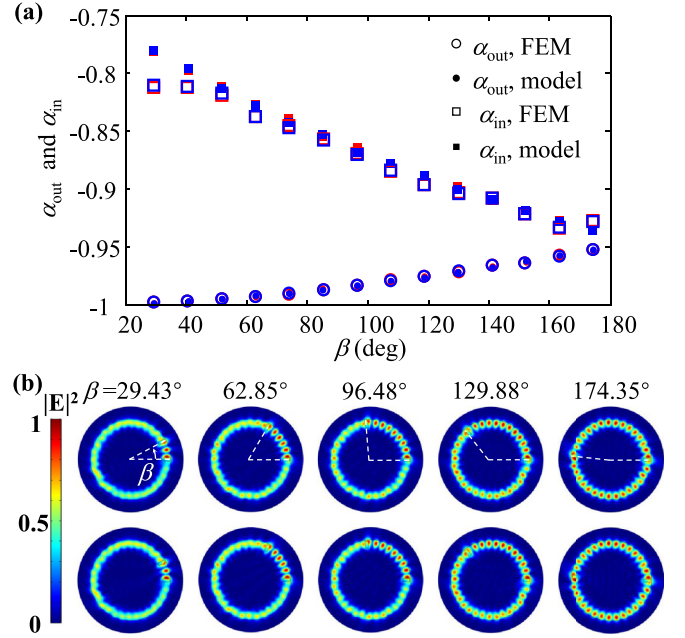


FIG. 3. (a) Chiralities $\alpha_{\text{out(in)}}$ at exceptional points (EPs) plotted as functions of β . The hollow (solid) circles and the squares denote the full-wave finite-element method (FEM) results (model predictions) of α_{out} and α_{in} , respectively. Blue and red correspond to two resonant modes. (b) Electric-field intensity distribution at the EPs for different β values corresponding to the FEM results shown in (a). The different columns are for different β , and the two rows are for the pair of nearly degenerate resonant modes.

To understand the locally imperfect or locally perfect chirality at EPs, we apply the APM multiple-scattering model [26] to the present case of strong scatterers.

Theoretical model. By considering a multiple-scattering process that incorporates the elastic transmission and reflection of APMs at the effective scatterer, a set of coupled-APM equations can be written as [26]

$$a_{\text{ccw}} = a_{\text{ccw}}wT + a_{\text{cw}}wR_{\text{ccw}}, \quad (4a)$$

$$a_{\text{cw}} = a_{\text{ccw}}wR_{\text{cw}} + a_{\text{cw}}wT, \quad (4b)$$

where T , R_{cw} , and R_{ccw} denote the effective scattering coefficients of the APMs at the effective scatterer as defined in Figs. 1(b1) and 1(b2). The effective scattering coefficients can be further derived from a Fabry-Pérot-like model [26]:

$$R_{\text{cw(ccw)}} = \rho_{1(2)} + \frac{v^2 \rho_{2(1)} \tau_{1(2)}^2}{1 - v^2 \rho_1 \rho_2}, \quad T = \frac{v \tau_1 \tau_2}{1 - v^2 \rho_1 \rho_2}, \quad (5)$$

where ρ_j and τ_j ($j = 1, 2$) denote the fundamental reflection and transmission coefficients of the APM at nanohole j , respectively [as defined in Figs. 1(d1) and 1(d2)]. Note that n_{eff} , ρ_j , and τ_j all weakly depend on the frequency ω [29]. Therefore, the frequency dependence of $R_{\text{cw(ccw)}}$ and T is dominated by the frequency dependence of $v = \exp(ik_0 n_{\text{eff}} R_0 \beta)$ which varies rapidly with the frequency ω via $k_0 = \omega/c$.

The complex resonance frequencies (eigenvalues) of the two split modes, denoted by ω_+ and ω_- , can be obtained by solving the nontrivial solution of Eq. (4). By setting the determinant of the coefficient matrix of Eq. (4) to zero, one

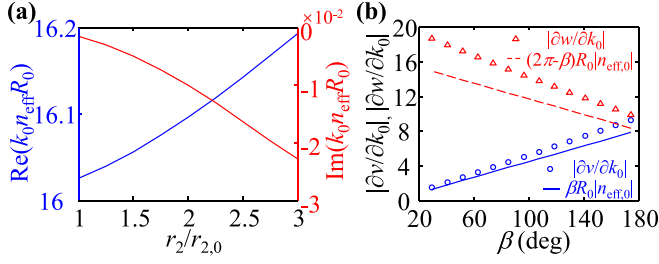


FIG. 4. (a) Real and imaginary parts of $k_0 n_{\text{eff}} R_0$ plotted as functions of the size r_2 of nanohole 2, which are obtained with the model at the exceptional points (EPs) already shown in Fig. 2. (b) $|\partial w/\partial k_0|$ (circles) and $|\partial v/\partial k_0|$ (triangles) at the EPs for the different β values already shown in Fig. 3. The solid and dashed curves show the results of $\beta R_0 |n_{\text{eff},0}|$ and $(2\pi - \beta) R_0 |n_{\text{eff},0}|$, respectively.

can determine the ω_+ and ω_- by solving two transcendental equations [26]:

$$w(\omega_{\pm}) = \frac{1}{T(\omega_{\pm}) \pm R(\omega_{\pm})}, \quad (6)$$

where $R(\omega) = \sqrt{R_{\text{cw}}(\omega) R_{\text{ccw}}(\omega)}$, and $R(\omega_+)$ [respectively, $-R(\omega_-)$] denotes one of the two single-valued branches of $R(\omega)$ at $\omega = \omega_+$ (respectively, $\omega = \omega_-$). The single-valued branches of $R(\omega_+)$ and $-R(\omega_-)$ for $\omega_+ \neq \omega_-$ have no specific relation for the present case of strong scatterers, which is different from $R(\omega_+) \approx R(\omega_-)$ for the case of weak scatterers [26].

Substituting Eq. (6) into Eq. (4), one can obtain the non-trivial solutions [26]:

$$\frac{a_{\text{ccw}}(\omega_{\pm})}{a_{\text{cw}}(\omega_{\pm})} = \pm \sqrt{\frac{R_{\text{ccw}}(\omega_{\pm})}{R_{\text{cw}}(\omega_{\pm})}}, \quad (7)$$

where a_{ccw} or a_{cw} is determined by the normalization of the resonant mode. In addition to the effective scatterer defined in Ref. [26], here, we further define a complementary effective scatterer with an azimuthal range from β to 2π as sketched in Figs. 1(c1) and 1(c2). The resultant merit is that $b_{\text{ccw}}/b_{\text{cw}}$ can be obtained in the same way as $a_{\text{ccw}}/a_{\text{cw}}$ with the following replacements in Eqs. (4)–(7), $a_{\text{cw}(\text{ccw})} \rightarrow b_{\text{cw}(\text{ccw})}$, $w \rightarrow v$, $v \rightarrow w$, $R_{\text{cw}(\text{ccw})} \rightarrow R'_{\text{cw}(\text{ccw})}$, $T \rightarrow T'$, $\rho_{1(2)} \rightarrow \rho_{2(1)}$, and $\tau_{1(2)} \rightarrow \tau_{2(1)}$ (see SM Secs. 2.1 and 2.2 [28]). This merit is crucial for explaining the local feature of the chirality at EPs.

With the solved $a_{\text{ccw}}/a_{\text{cw}}$ and $b_{\text{ccw}}/b_{\text{cw}}$ inserted into Eq. (3), the local chiralities outside and inside the effective scatterer can be expressed as

$$\alpha_{\text{out}} \approx \frac{|R_{\text{ccw}}| - |R_{\text{cw}}|}{|R_{\text{ccw}}| + |R_{\text{cw}}|}, \quad \alpha_{\text{in}} \approx \frac{|R'_{\text{ccw}}| - |R'_{\text{cw}}|}{|R'_{\text{ccw}}| + |R'_{\text{cw}}|}, \quad (8)$$

respectively, where $|v| \approx |w| \approx 1$ in view of $\text{Im}(k_0 n_{\text{eff}} R_0) \approx 0$ [see Fig. 4(a)]. Equation (8) indicates that a perfect chirality $|\alpha_{\text{out}}| = 1$ ($|\alpha_{\text{in}}| = 1$) is equivalent to a unidirectional no reflection of APM at the (complementary) effective scatterer, i.e., $R_{\text{cw}} = 0$ or $R_{\text{ccw}} = 0$ ($R'_{\text{cw}} = 0$ or $R'_{\text{ccw}} = 0$).

Validity of the model. For the model predictions, the EPs are obtained by simultaneously scanning r_1 and β with the other parameters being the same as the FEM results. As shown in Figs. 2 and 3, the chiralities predicted by the model agree

well with those obtained with the full-wave FEM. More results to validate the model can be found in SM Secs. 2.3 and 2.4 [28].

Explanation of the conditional globally perfect chirality at EPs. The shifts of complex resonance frequencies of the two split resonant modes induced by the weak scatterers are quite small. It implies $k_0 n_{\text{eff}} R_0 \approx m$ [as confirmed numerically in Fig. 4(a)] and $\omega_+ \approx \omega_- \approx \omega_0$ (ω_0 being the complex resonance frequency for the unperturbed WGM).

Therefore, for the case of weak scatterers, the effective scattering coefficients $R_{\text{cw}(\text{ccw})}$ and T are approximately independent of the frequency ω due to $v \approx \exp(im\beta)$ and the weak dependence of ρ_j and τ_j on ω [see Eq. (5)]. Then Eq. (6) becomes

$$w(\omega_{\pm}) = \frac{1}{T \pm R}, \quad (9)$$

where R and $-R$ denote the two single-valued branches of $\sqrt{R_{\text{cw}} R_{\text{ccw}}}$ that is approximately independent of ω . This implies that R and $-R$ become related, which is different from the general situation in Eq. (6). When the system is steered to the EP, there is $w(\omega_+) = w(\omega_-)$ due to the degeneracy of the eigenfrequency ($\omega_+ = \omega_-$), which yields $R = 0$, i.e., R being at the square-root branch point [2,34]. Consequently, there is $R_{\text{cw}} = 0$ or $R_{\text{ccw}} = 0$ at the EP, which will result in a perfect local chirality $|\alpha_{\text{out}}| = 1$ according to Eq. (8).

Similarly, $R'_{\text{cw}(\text{ccw})}$ and T' are approximately independent of ω due to $w \approx \exp[im(2\pi - \beta)]$ for weak scatterers. Analogous to Eq. (9), one can obtain

$$v(\omega_{\pm}) = \frac{1}{T' \pm R'}, \quad (10)$$

by considering the complementary effective scatterer, where $R' = \sqrt{R'_{\text{cw}} R'_{\text{ccw}}}$. Consequently, there is $R' = 0$, i.e., $R'_{\text{cw}} = 0$ or $R'_{\text{ccw}} = 0$ at the EP, which causes a perfect local chirality $|\alpha_{\text{in}}| = 1$. Additionally, it can be proved that $b_{\text{cw}(\text{ccw})} \approx 0$ if $R_{\text{cw}(\text{ccw})} = 0$ for weak scatterers [26], which results in a globally perfect chirality ($\alpha_{\text{out}} \approx \alpha_{\text{in}} \approx \pm 1$) at the EP. This is consistent with the prediction by the approach using an effective frequency-independent non-Hermitian Hamiltonian matrix upon the basis of CW and CCW WGMs [19].

Explanation of the conditional locally perfect chirality at EPs. For the case of strong scatterers, the frequency dependence of $[R_{\text{cw}(\text{ccw})}, T]$ and $[R'_{\text{cw}(\text{ccw})}, T']$ (dominated by the frequency dependence of v and w , respectively) could be remarkably different, which will result in the locally perfect chirality at EPs. This can be understood in view of

$$\left| \frac{\partial v}{\partial k_0} \right| = \beta R_0 \left| \frac{\partial(k_0 n_{\text{eff}})}{\partial k_0} \right| |v| \approx \beta R_0 |n_{\text{eff}}|, \quad (11)$$

and

$$\left| \frac{\partial w}{\partial k_0} \right| = (2\pi - \beta) R_0 \left| \frac{\partial(k_0 n_{\text{eff}})}{\partial k_0} \right| |w| \approx (2\pi - \beta) R_0 |n_{\text{eff}}|, \quad (12)$$

where $|\partial(k_0 n_{\text{eff}})/\partial k_0| \approx |n_{\text{eff}}|$ due to the weak dependence of n_{eff} on ω . Equation (11) indicates that $|\partial v/\partial k_0|$ tends to be 0 with the decrease of β , which means a weaker dependence of $R_{\text{cw}(\text{ccw})}$ and T on ω . Consequently, Eq. (9) holds which leads to $|\alpha_{\text{out}}| = 1$ for small β , as shown in Fig. 3(a). Differently,

$|\partial w/\partial k_0|$ increases with the decrease of β , which means a strong dependence of $R'_{\text{cw}}(\text{ccw})$ and T' on ω . Thus, Eq. (10) does not hold which results in $|\alpha_{\text{in}}| < 1$ for large β , as shown in Fig. 3(a). The validity of Eqs. (11) and (12) is confirmed in Fig. 4(b), where n_{eff} approximately takes $n_{\text{eff},0} = 1.6186 + 9.9531 \times 10^{-6}i$ for the unperturbed WGM. The evolution of reflection coefficients $R_{\text{cw}(\text{ccw})}$ and $R'_{\text{cw}(\text{ccw})}$ near the EP can be found in SM Sec. 4 [28].

This locally perfect chirality can be seen as reasonable in view that the effective scatterer is generally azimuthally asymmetric and different from the complementary effective scatterer (with some exceptions, e.g., two identical scatterers with $\beta = \pi$), which will lead to different reflection coefficients [$R_{\text{cw}(\text{ccw})} \neq R'_{\text{cw}(\text{ccw})}$] of the APMs. In addition to the above explanation, a logic crosscheck on the locally perfect chirality can be found in SM Sec. 3 [28].

Following the above explanation, $|\alpha_{\text{out}}| > |\alpha_{\text{in}}|$, as shown in Fig. 2(a), can be understood in view of the smaller relative azimuthal angle of the effective scatterer ($\beta \approx 130^\circ$) than that of the complementary effective scatterer ($2\pi - \beta \approx 230^\circ$).

The imperfect and local features of the chirality at EP for strong scatterers could probably also be explained by enlarging the dimensionality (>2) of the effective non-Hermitian Hamiltonian [19] by considering > 2 CW and CCW WGMs as the basis.

Conclusions. In this letter, we reveal that the chirality of the resonant modes at EPs of a WGM microcavity perturbed by two strong nanoscaters is generally local and imperfect. The chirality will tend to be globally perfect for weak scatterers or locally perfect for small relative azimuthal angle between the two scatterers. With a first-principles-based model that incorporates an intuitive multiple-scattering process of the APMs, the conditional appearance of perfect local chirality at EPs is attributed to the weak frequency dependence of the effective APM scattering coefficients

at the effective scatterer, and correspondingly, the general imperfect local chirality at EPs is due to the strong frequency dependence of the effective APM scattering coefficients. Consequently, a stronger local chirality at EPs is observed in the larger azimuthal region divided by the two scatterers.

The local chirality could be measured experimentally in a microcavity system with two coupling waveguides, respectively, located in the larger and smaller azimuthal ranges divided by the two scatterers (see Fig. S10 in SM Sec. 6 [28]). By measuring the intensities of the outgoing eigenmodes (for instance, lasing) from the two sides of each of the two waveguides, one can obtain the intensities of the CW or CCW traveling waves in the larger and smaller azimuthal ranges divided by the two scatterers and then obtain the local chiralities (see Eq. (S16) in SM Sec. 6 [28]).

The discovered general features of the local chirality at the EP will enrich the understanding of EPs, not only in optics but also in other systems, such as microwave [16], acoustic [35], and quantum systems [36]. The previous criterion of an EP in experiments [8,20,25], i.e., a globally perfect chirality or the equivalent unidirectional no reflection [see Eq. (8)], should be refreshed for strong scatterers. Additionally, the proposed peculiar features of the chirality at the EP may promote unconventional applications in the on-chip chiral photonics, for instance, an optional unidirectional or bidirectional lasing in different azimuthal ranges of the microcavity based on the locally perfect chirality at the EP (see SM Sec. 6 [28]).

Acknowledgments. Financial support from the National Key Research and Development Program of China (No. 2022YFA1404602), National Natural Science Foundation of China (No. 92250302, No. 62075104, No. 12034010, No. 12134007, No. 92050111, and No. 12074199), and 111 Project (No. B23045) is acknowledged.

-
- [1] T. Kato, *Perturbation Theory for Linear Operators* (Springer-Verlag, Berlin, 1995).
 - [2] W. D. Heiss, The physics of exceptional points, *J. Phys. A* **45**, 444016 (2012).
 - [3] H. Cartarius, J. Main, and G. Wunner, Exceptional points in atomic spectra, *Phys. Rev. Lett.* **99**, 173003 (2007).
 - [4] Y. Choi, S. Kang, S. Lim, W. Kim, J. R. Kim, J. H. Lee, and K. An, Quasieigenstate coalescence in an atom-cavity quantum composite, *Phys. Rev. Lett.* **104**, 153601 (2010).
 - [5] Y. X. Shen, Y. G. Peng, D. G. Zhao, X. C. Chen, J. Zhu, and X. F. Zhu, One-way localized adiabatic passage in an acoustic system, *Phys. Rev. Lett.* **122**, 094501 (2019).
 - [6] M. A. Miri and A. Alu, Exceptional points in optics and photonics, *Science* **363**, eaar7709 (2019).
 - [7] H. Xu, D. Mason, L. Jiang, and J. G. Harris, Topological energy transfer in an optomechanical system with exceptional points, *Nature (London)* **537**, 80 (2016).
 - [8] W. J. Chen, S. K. Ozdemir, G. M. Zhao, J. Wiersig, and L. Yang, Exceptional points enhance sensing in an optical microcavity, *Nature (London)* **548**, 192 (2017).
 - [9] H. Hodaie, A. U. Hassan, S. Wittek, H. Garcia-Gracia, R. El-Ganainy, D. N. Christodoulides, and M. Khajavikhan, Enhanced sensitivity at higher-order exceptional points, *Nature (London)* **548**, 187 (2017).
 - [10] J.-H. Park, A. Ndao, W. Cai, L. Hsu, A. Kodigala, T. Lepetit, Y.-H. Lo, and B. Kanté, Symmetry-breaking-induced plasmonic exceptional points and nanoscale sensing, *Nat. Phys.* **16**, 462 (2020).
 - [11] J. Zhang, B. Peng, Ş. K. Özdemir, K. Pichler, D. O. Krimer, G. Zhao, F. Nori, Y.-x. Liu, S. Rotter, and L. Yang, A phonon laser operating at an exceptional point, *Nat. Photonics* **12**, 479 (2018).
 - [12] J. Doppler, A. A. Mailybaev, J. Böhm, U. Kuhl, A. Girschik, F. Libisch, T. J. Milburn, P. Rabl, N. Moiseyev, and S. Rotter, Dynamically encircling an exceptional point for asymmetric mode switching, *Nature (London)* **537**, 76 (2016).
 - [13] X.-L. Zhang, S. Wang, B. Hou, and C. T. Chan, Dynamically encircling exceptional points: *In situ* control of encircling loops and the role of the starting point, *Phys. Rev. X* **8**, 021066 (2018).

- [14] X. Shu, A. Li, G. Hu, J. Wang, A. Alu, and L. Chen, Fast encirclement of an exceptional point for highly efficient and compact chiral mode converters, *Nat. Commun.* **13**, 2123 (2022).
- [15] W. D. Heiss and H. L. Harney, The chirality of exceptional points, *Eur. Phys. J. D* **17**, 149 (2001).
- [16] C. Dembowski, B. Dietz, H. D. Graf, H. L. Harney, A. Heine, W. D. Heiss, and A. Richter, Observation of a chiral state in a microwave cavity, *Phys. Rev. Lett.* **90**, 034101 (2003).
- [17] J. Wiersig, A. Eberspächer, J.-B. Shim, J.-W. Ryu, S. Shinohara, M. Hentschel, and H. Schomerus, Nonorthogonal pairs of co-propagating optical modes in deformed microdisk cavities, *Phys. Rev. A* **84**, 023845 (2011).
- [18] P. Miao, Z. F. Zhang, J. B. Sun, W. Walasik, S. Longhi, N. M. Litchinitser, and L. Feng, Orbital angular momentum micro-laser, *Science* **353**, 464 (2016).
- [19] J. Wiersig, Structure of whispering-gallery modes in optical microdisks perturbed by nanoparticles, *Phys. Rev. A* **84**, 063828 (2011).
- [20] B. Peng, S. K. Ozdemir, M. Liertzer, W. J. Chen, J. Kramer, H. Yilmaz, J. Wiersig, S. Rotter, and L. Yang, Chiral modes and directional lasing at exceptional points, *Proc. Natl. Acad. Sci. USA* **113**, 6845 (2016).
- [21] W. R. Sweeney, C. W. Hsu, S. Rotter, and A. D. Stone, Perfectly absorbing exceptional points and chiral absorbers, *Phys. Rev. Lett.* **122**, 093901 (2019).
- [22] S. Soleymani, Q. Zhong, M. Mokim, S. Rotter, R. El-Ganainy, and S. K. Ozdemir, Chiral and degenerate perfect absorption on exceptional surfaces, *Nat. Commun.* **13**, 599 (2022).
- [23] C. Wang, X. Jiang, G. Zhao, M. Zhang, C. W. Hsu, B. Peng, A. D. Stone, L. Jiang, and L. Yang, Electromagnetically induced transparency at a chiral exceptional point, *Nat. Phys.* **16**, 334 (2020).
- [24] C. Wang, X. Jiang, W. R. Sweeney, C. W. Hsu, Y. Liu, G. Zhao, B. Peng, M. Zhang, L. Jiang, A. D. Stone *et al.*, Induced transparency by interference or polarization, *Proc. Natl. Acad. Sci. USA* **118**, e2012982118 (2021).
- [25] C. Wang, W. R. Sweeney, A. D. Stone, and L. Yang, Coherent perfect absorption at an exceptional point, *Science* **373**, 1261 (2021).
- [26] J. Zhu, H. Liu, F. Bo, C. Tao, G. Zhang, and J. Xu, Intuitive model of exceptional points in an optical whispering-gallery microcavity perturbed by nanoparticles, *Phys. Rev. A* **101**, 053842 (2020).
- [27] J. Wiersig, Sensors operating at exceptional points: General theory, *Phys. Rev. A* **93**, 033809 (2016).
- [28] See Supplemental Material at <http://link.aps.org/supplemental/10.1103/PhysRevA.108.L041501> for some details on the dependence of the scattering coefficients on the location, refractive index, and size of the nanoscatterer; additional logic and numerical test on the validity of the model; some additional explanation of the conditional perfect chirality at EPs; evolution of reflection coefficients as functions of the relative azimuthal angle β between the two nanoholes; additional results of the electric-field intensities at the EPs for different β ; and simulation results showing the feasibility of an experimental demonstration of the theory.
- [29] J. Zhu, Y. Zhong, and H. Liu, Impact of nanoparticle-induced scattering of an azimuthally propagating mode on the resonance of whispering gallery microcavities, *Photonics Res.* **5**, 396 (2017).
- [30] P. Lalanne, W. Yan, K. Vynck, C. Sauvan, and J. P. Hugonin, Light interaction with photonic and plasmonic resonances, *Laser Photonics Rev.* **12**, 1700113 (2018).
- [31] J. Ren, S. Franke, and S. Hughes, Quasinormal modes, local density of states, and classical Purcell factors for coupled loss-gain resonators, *Phys. Rev. X* **11**, 041020 (2021).
- [32] L. Rayleigh, *Theory of Sound* (MacMillan, London, 1878), Vol. II.
- [33] C. Vassallo, *Optical Waveguide Concepts* (Elsevier, Amsterdam, 1991).
- [34] C. Dembowski, H. D. Graf, H. L. Harney, A. Heine, W. D. Heiss, H. Rehfeld, and A. Richter, Experimental observation of the topological structure of exceptional points, *Phys. Rev. Lett.* **86**, 787 (2001).
- [35] H. Z. Chen, T. Liu, H. Y. Luan, R.-J. Liu, X.-Y. Wang, X.-F. Zhu, Y.-B. Li, Z.-M. Gu, S.-J. Liang, H. Gao *et al.*, Revealing the missing dimension at an exceptional point, *Nat. Phys.* **16**, 571 (2020).
- [36] T. Gao, G. Li, E. Estrecho, T. C. H. Liew, D. Comber-Todd, A. Nalitov, M. Steger, K. West, L. Pfeiffer, D. W. Snoke *et al.*, Chiral modes at exceptional points in exciton-polariton quantum fluids, *Phys. Rev. Lett.* **120**, 065301 (2018).